

Composition dependence of intrinsic surface states and Fermi level pinning at ternary $\text{Al}_x\text{Ga}_{1-x}\text{N}$ m -plane surfaces

Lars Freter,¹ Liverios Lymperakis,^{2,3} Michael Schnedler,¹ Holger Eisele,⁴ Lei Jin,¹ Jianxun Liu,⁵ Qian Sun,⁵ Rafal E. Dunin-Borkowski,¹ and Philipp Ebert¹

¹*Ernst Ruska-Centrum (ER-C 1) and Peter Grünberg Institut (PGI 5), Forschungszentrum Jülich GmbH, 52425 Jülich, Germany*

²*Department of Physics, University of Crete, GR-70013 Heraklion, Greece*

³*Computational Materials Design Department, Max-Planck Institut für Eisenforschung GmbH, 40237 Düsseldorf, Germany*

⁴*Institut für Physik, Otto-von-Guericke-Universität Magdeburg, Universitätsplatz 2, 39106 Magdeburg, Germany*

⁵*Key Laboratory of Nano-devices and Applications, Suzhou Institute of Nano-Tech and Nano-Bionics, Chinese Academy of Sciences (CAS), Suzhou 215123, China*

Growth on non-polar group III-nitride semiconductor surfaces has been suggested to be a remedy for avoiding detrimental polarization effects. However, the presence of intrinsic surface states within the fundamental band gap at non-polar surfaces leads to a Fermi level pinning during growth, affecting incorporation of dopants and impurities. This is further complicated by the use of ternary e.g. $\text{Al}_x\text{Ga}_{1-x}\text{N}$ layers in device structures. In order to quantify the Fermi level pinning on ternary group III nitride non-polar growth surface, the energy position of the group III-derived empty dangling bond surface state at non-polar $\text{Al}_x\text{Ga}_{1-x}\text{N}(10\bar{1}0)$ surfaces is determined as a function of the Al concentration using cross-sectional scanning tunneling microscopy and spectroscopy. The measurements show that the minimum energy of the empty dangling bond state shifts linearly toward midgap for increasing Al concentration with a slope of $\approx 5\text{ meV}/\%$. These experimental findings are supported by complementary DFT calculations.

I. INTRODUCTION

Ternary $\text{Al}_x\text{Ga}_{1-x}\text{N}$ alloys are widely used in diverse applications of group III-nitride semiconductors, such as barriers or active media in multi quantum well (MQW)-based light emitting devices¹, from the visible to far uv spectral range, gate contacts in high power heterojunction field-effect transistors,² or strain engineering (buffer) layers of group III nitrides on silicon.^{3–6} In many of these devices polarization charges at heterointerfaces⁷ lead to sometimes desired but mostly detrimental effects such as charge separation in active MQW layers or two dimensional sheet charges in transistors. To avoid unwanted polarization effects, growth on semipolar and non-polar substrate orientations has been proposed as solution.^{8,9} However, even though non-polar surfaces are free of polarization charges, intrinsic surface states within the fundamental band gap of nitride semiconductors¹⁰ give rise to surface potentials with similar disadvantages.¹¹ For example, Fermi-level pinning by the empty Ga-derived dangling bond state on GaN $\{10\bar{1}0\}$ surfaces was found to create a surface potential of $\sim 0.7\text{ V}$.^{12–21}

However, despite their relevance for device fabrication, so far, only the surface states of GaN^{12,14}, InN²², and $\text{Al}_{0.8}\text{In}_{0.2}\text{N}$ ²³ non-polar surfaces have been thoroughly investigated, while those of other ternary compounds remain unknown. Therefore, we investigate here the composition dependence of intrinsic surface states and Fermi-level pinning at ternary $\text{Al}_x\text{Ga}_{1-x}\text{N}$ m -plane surfaces by a combination of cross-sectional scanning tunneling microscopy (XSTM) and cross-sectional scanning tunneling spectroscopy (XSTS) as well as density functional theory (DFT) calculations.

II. EXPERIMENT

The investigated sample structure consists of two ternary $\text{Al}_x\text{Ga}_{1-x}\text{N}$ layers with step-graded Al contents ($x = 0.17, 0.35$) and thicknesses (370 nm, 320 nm) on top of a 300 nm thick AlN buffer layer. All layers were grown by metal organic chemical vapor phase deposition (MOCVD) on a Si(111) substrate.²⁴ Secondary ion mass spectrometry (SIMS) indicates a Si dopant concentration in the low 10^{18} cm^{-3} range, without concentration gradient within each of the three layers.

For the XSTM/XSTS investigations, small rectangular samples were cut from the as-grown wafer, thinned, and electrically contacted (using sputtered Au layers).²⁴ After transfer into an ultrahigh vacuum chamber ($p < 2 \cdot 10^{-8}\text{ Pa}$) the samples were cleaved to obtain contamination-free cross-sectional $(10\bar{1}0)$ surfaces. The XSTM and XSTS measurements were performed without interruption of the vacuum, using electro-chemically etched tungsten tips.

Compositions and layer thicknesses were studied by energy dispersive x-ray (EDX) spectroscopy in a FEI Titan G2 80-200 CREWLEY scanning transmission electron microscope (STEM).^{24,25} Since the measured and nominal ternary (Al,Ga)N compositions are very close considering the measurement accuracy, we use the nominal compositions for labeling the layers in the following.

III. RESULTS

Figure 1 provides a microscopic, electronic, and chemical overview of the $\text{Al}_{0.17}\text{Ga}_{0.83}\text{N}/\text{Al}_{0.35}\text{Ga}_{0.65}\text{N}/\text{AlN}/\text{Si}$

heterostructure. The constant-current XSTM image in Fig. 1(a) illustrates the topography of the non-polar (10 $\bar{1}0$) cleavage surface in a cross-sectional view through the heterostructure. The topography is characterized by large atomically flat terraces separated by cleavage steps of various heights with a density of $(3-5) \times 10^4 \text{ cm}^{-2}$. At the heterointerfaces no change in topography can be discerned, despite the rather large compositional changes [cf. Fig. 1(c)]. In particular, the cleavage steps cross the interfaces without any directional change. Only in the far left bottom corner of the constant-current STM image the outermost edge of the Si substrate, which is not of interest here, induces a change in cleavage orientation and subsequently a large height change.

Current imaging tunneling spectroscopy (CITS) maps evaluated at negative sample voltages (not shown here) reveal no detectable electronic contrast change at the $\text{Al}_{0.35}\text{Ga}_{0.65}\text{N}/\text{AlN}$ and $\text{Al}_{0.17}\text{Ga}_{0.83}\text{N}/\text{Al}_{0.35}\text{Ga}_{0.65}\text{N}$ heterointerfaces. In contrast, CITS maps evaluated at positive sample voltages [Fig. 1(b)] reveal a notable change of current-induced contrast at the $\text{Al}_{0.35}\text{Ga}_{0.65}\text{N}/\text{AlN}$ interface (cf. left dashed white line), whereas the electronic change at the $\text{Al}_{0.17}\text{Ga}_{0.83}\text{N}/\text{Al}_{0.35}\text{Ga}_{0.65}\text{N}$ interface with smaller composition change is almost absent. Therefore, we determined the spatial position of this latter $\text{Al}_{0.17}\text{Ga}_{0.83}\text{N}/\text{Al}_{0.35}\text{Ga}_{0.65}\text{N}$ interface in the XSTM image and CITS map using the $\text{Al}_{0.35}\text{Ga}_{0.65}\text{N}$ layer thickness as obtained by EDX (cf. right white dashed lines), relative to the $\text{Al}_{0.35}\text{Ga}_{0.65}\text{N}/\text{AlN}$ interface position identified in the CITS maps.

Note, the curved stripe contrast within the (Al,Ga)N layers are step-related features attributable to step-induced states, whereas the horizontal single pixel wide lines arise from tip-instabilities.

At this stage we turn to current-voltage spectra acquired at different spatial positions on the cross-sectional cleavage surface marked by filled circles in Fig. 1(a). Figure 2 (a) and (b) show averages of all tunneling spectra acquired at spatial positions within the $\text{Al}_{0.17}\text{Ga}_{0.83}\text{N}$ and $\text{Al}_{0.35}\text{Ga}_{0.65}\text{N}$ layers, far enough from the interfaces, in blue and red symbols, respectively. The error bars reveal that the spectra and the electronic properties are homogeneous throughout each (Al,Ga)N layer. In contrast, within the AlN layer the tunneling spectra exhibit a pronounced dependence along the growth direction. This is illustrated with three averaged spectra, acquired within the AlN layer but with increasing distances from the $\text{Al}_{0.35}\text{Ga}_{0.65}\text{N}/\text{AlN}$ interface in Fig. 2(c). Their spatial positions are numbered correspondingly as in Fig. 1(a).

Figure 2 illustrates that the negative voltage branches of all spectra of the three layers exhibit identical onset voltages and slopes, in line with the lack of any contrast at the interfaces in filled states images [see Fig. 1(a)]. In contrast, at positive voltages the onsets increase with the Al concentration, whereas the slopes decreases.

Within the AlN layer a rather large systematic change of the spectra occurs in addition: The AlN spectra ex-

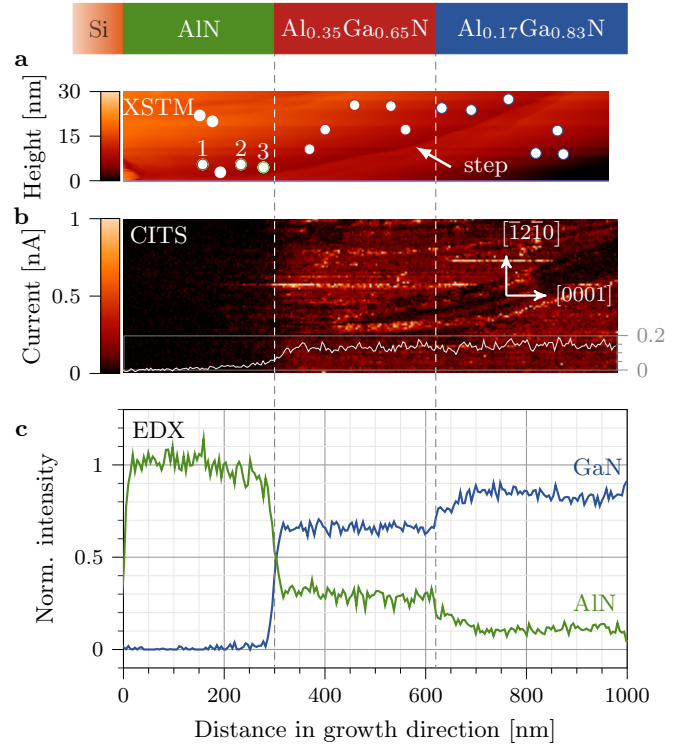


Figure 1. (a) Constant-current XSTM image, measured at a setpoint of -2.5 V and 80 pA , revealing atomic terraces separated by steps. The white dots correspond to the acquisition positions of sets of 25 tunneling spectra each used in Fig. 2. (b) CITS map acquired in an adjacent area. The CITS map depicts the measured current at a selected voltage of $+4.8 \text{ V}$. The tip-sample separation is fixed by a setpoint of -4.5 V and 80 pA . The white overlay in the bottom region shows a line profile in $[0001]$ direction of the current in nA (right scale) at voltage of $+4.8 \text{ V}$ extracted from the CITS map. (c) Al and Ga composition profiles along the $[0001]$ growth direction measured by EDX taken from Ref.²⁴, revealing the interface positions between the three layers of interest. While the XSTM image in (b) does not reveal topographic changes at the heterointerfaces, the CITS image in (c) exhibits a pronounced (vanishing) change of contrast and thus of the electronic properties at the $\text{Al}_{0.35}\text{Ga}_{0.65}\text{N}/\text{AlN}$ ($\text{Al}_{0.17}\text{Ga}_{0.83}\text{N}/\text{Al}_{0.35}\text{Ga}_{0.65}\text{N}$) interface.

hibit a shift to larger onset voltages with increasing distance to the $\text{Al}_{0.35}\text{Ga}_{0.65}\text{N}/\text{AlN}$ interface [cf. Fig. 2(c)]. Therefore, we first consider in the discussion below spectra measured in the center of the AlN layer, i.e. far away from the $\text{AlN}/\text{Al}_{0.35}\text{Ga}_{0.65}\text{N}$ interface [dark green symbols in Fig. 2(c)]. Later on we address the systematic shifts. The two ternary (Al,Ga)N layers exhibit no such spatial variation of the tunneling spectra.

IV. DISCUSSION

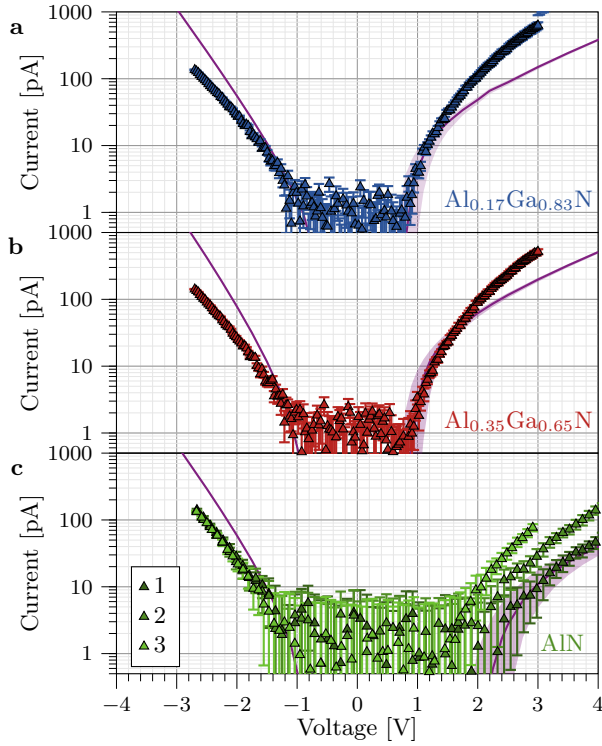


Figure 2. Current-voltage $I(V)$ tunnel spectra measured on (a) the $\text{Al}_{0.17}\text{Ga}_{0.83}\text{N}$ layer (blue symbols), (b) the $\text{Al}_{0.35}\text{Ga}_{0.65}\text{N}$ layer (red symbols), and (c) the AlN layer (green symbols) at three different spatial positions visible in Fig. 1a. All spectra were obtained using the same setpoint (-2.5 V and 80 pA). The onset of the spectra were fitted by adjusting the surface state energy level in the simulation as described in the text^{26–28} (violet lines). The violet shading illustrates the range induced by a $\pm 0.2\text{ eV}$ and $\pm 0.4\text{ eV}$ change of the surface state position of (Al,Ga)N and AlN, respectively.

A. Surface band bending

In order to understand the Al composition-dependent current onsets at positive voltages (and the lack of Al concentration dependence at negative voltages), we recall that clean $\text{GaN}(10\bar{1}0)$ surfaces exhibit filled dangling bonds localized at the surface N atoms and empty dangling bonds above the surface Ga atoms. Both types of dangling bonds point into the vacuum.¹² Unlike non-polar surfaces of zincblende III-V semiconductors, where all surface states are found to be outside of the fundamental band gap,²⁹ the empty Ga-derived dangling bond of $\text{GaN}(10\bar{1}0)$ is energetically located in the upper part of the fundamental band gap.^{12–21}

The presence of the empty dangling bond state within the band gap induces an upward band bending and becomes partially occupied on n -type surfaces. Due to the high density of the Ga-derived surface state its lowermost tail of the LDOS in the band gap is pinned at the Fermi level (so-called Fermi-level pinning). Hence, the

magnitude of the band bending reflects the energy separation between the minimum of the surface state and the conduction band edge in highly n -doped GaN. Note, the density of step states can be estimated to about 10^{12} cm^{-2} on basis of the measured step density. This value is much lower than the density of intrinsic surface states of $6.2 \times 10^{14}\text{ cm}^{-2}$, which thus dominates Fermi level pinning.

In an STM setup, the additional presence of a biased probe tip modifies this intrinsic band bending: At positive voltages, this additional electric field increases the intrinsic band bending primarily at large voltages only, where the tip-induced band bending dominates. At small positive voltages, the tip-induced band bending is negligible and therefore only the intrinsic band bending due to the partial occupation of the minimum of the empty surface state in the band gap (i.e. Fermi level pinning) governs the tunnel current onset.¹⁵ Thus the onset of the positive voltage branch of the $I(V)$ curves is indicative of the position of the intrinsic surface state in the band gap.¹⁵

At negative voltages, the tip attempts to induce a downward band bending. However the density of the Ga-derived surface state is too large and therefore the partially occupied surface state cannot be fully filled. Hence the Fermi-level pinning at the Ga-derived surface state energy prevails. As outlined previously, this is apparently in conflict with the onset of the negative current branch.¹⁵ The apparent conflict can be resolved by considering the tunneling currents themselves. Under tunneling conditions with negative sample voltages applied, the electrons tunnel from the partially filled Ga-derived surface state into the tip states. Due to the particular electronic structure of the conduction band minimum and the Ga-derived surface state, the electrons from the conduction band cannot refill the surface state at a sufficient rate.¹⁵ Hence under tunneling conditions the surface state is emptied and does not influence the tip-induced band bending. Instead the conduction band edge is dragged below the Fermi energy, creating an electron accumulation zone in the conduction band. This accumulation zone is at the origin of the strong tunnel current into the tip starting already at small negative sample voltages. The accumulation current is independent of the energy position of the surface state.

For the ternary $\text{Al}_{0.17}\text{Ga}_{0.83}\text{N}$ and $\text{Al}_{0.35}\text{Ga}_{0.65}\text{N}$ ($10\bar{1}0$) cleavage surfaces an analogous surface structure is obtained by theory (see calculations below). Hence the tunnel current onsets can be interpreted on the basis of the accumulation current (negative current branch) and the energy position of the cation-derived dangling bond state in the band gap (positive current branch).

The onset of the accumulation current is in first approximation solely determined by the energy difference between the Fermi level and the conduction band minimum. Since all layers in the heterostructure are n -doped, they will have almost identical Fermi level positions with respect to the conduction band and thus the resulting

current and its onset can be anticipated to be essentially independent of the Al composition. Thus the contrast of filled state images is dominated by topographic features only, explaining the lack of electronic contrast at the heterointerfaces in the XSTM images acquired at negative voltages.

B. Simulation of the tunnel current

1. $\text{Al}_x\text{Ga}_{1-x}\text{N}$ layers

Based on the electronic surface structure and tunneling model, we simulated the tunnel currents of the two ternary $\text{Al}_{0.17}\text{Ga}_{0.83}\text{N}$ and $\text{Al}_{0.35}\text{Ga}_{0.65}\text{N}$ (10 $\bar{1}0$) cleavage surfaces. For the simulation of the tunnel currents the relevant material parameters of the ternary alloys (electron affinity, dielectric constant) were approximated by Vegard's law from the binary compounds. The effective mass and the donor ionization energy, were approximated by the values of GaN, since in the used composition range almost no changes occur.^{30–34} The Si doping concentration in both ternary layers was estimated on basis of SIMS data to $1.6 \cdot 10^{18} \text{ cm}^{-3}$ with the assumption of no doping compensation.^{33–35}

The minimum of the empty cation-derived surface state is modeled as Gaussian distribution with a full width at half maximum of 0.1 eV and a surface state density of $6 \times 10^{14} \text{ cm}^{-2}$. Note, only the lowermost tail below the Fermi level is occupied, yielding a surface charge density in the range of 10^{12} – 10^{13} cm^{-2} . The centroid energy of the Gaussian distribution E_{pin} was used as fit parameter and represents the minimum of the surface state's LDOS. Note, since only the lowermost DOS of the surface state is populated and thereby inducing the Fermi level pinning, it is sufficient to include only this lowermost DOS in the electrostatic calculation. The higher states of the dispersing surface state extend into the conduction band, but are not relevant for Fermi level pinning. A standard probe tip with a 60 nm radius, an apex opening angle of 45° , and a work function of 4.0 eV^{36–39} was used in all simulations. The electron affinities of the ternary compounds are determined on basis of the respective values of the binary compounds using Vegard's law, since an almost linear dependence of the electron affinity on the Al composition has been observed.^{40–42} For the non-polar GaN(10 $\bar{1}0$) surface an experimental value of 4.1 eV is used.⁴³ For the non-polar AlN(10 $\bar{1}0$) surface no experimental data is available and we turned to theoretical calculations, which yielded an electron affinity 2.3 eV smaller than that of GaN(10 $\bar{1}0$).⁴⁴ This is compatible with the values in the upper range of the electron affinity for polar AlN surfaces of 0.6 eV to 2.0 eV.^{40,41,45–49} Thus, electron affinities of $\chi = 3.74 \text{ eV}$ and 3.37 eV are used for the two ternary $\text{Al}_{0.17}\text{Ga}_{0.83}\text{N}$ and $\text{Al}_{0.35}\text{Ga}_{0.65}\text{N}$ (10 $\bar{1}0$) cleavage surfaces, respectively.

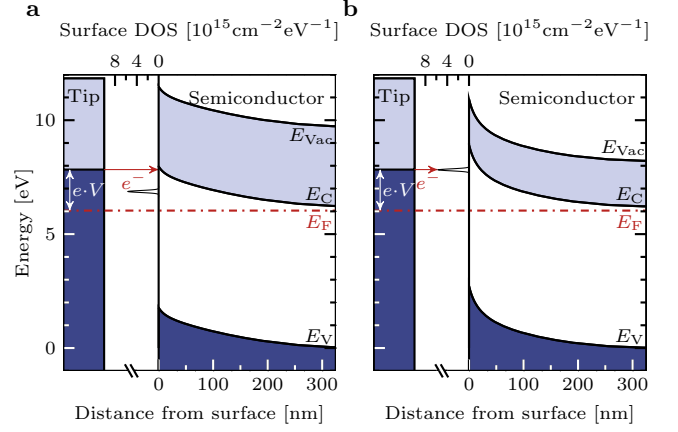


Figure 3. Band diagrams for (a) tunneling only into bulk states (at large electron affinity) and (b) tunneling into the minimum of the empty surface state (at small electron affinity) illustrated for the onset voltage of the positive current branch. Note tunneling at onset voltages occurs only into the minimum the empty surface state, which is therefore illustrated as Gaussian in first approximation.

The violet solid lines in Fig. 2 show the best agreeing simulated tunnel spectra in comparison to the measured $I(V)$ curves. In case of the ternary nitride layers, the best agreement is achieved for minima of the empty surface state of $E_C - (0.7 \pm 0.2) \text{ eV}$ and $E_C - (0.8 \pm 0.2) \text{ eV}$ for Al contents of 17%, and 35%, respectively. The violet shaded areas in Fig. 2 indicate the range of the simulated $I(V)$ curves that correspond to the respective uncertainties.

2. AlN layer

At this stage we turn to the pure AlN(10 $\bar{1}0$) surface. First, we assume that the electronic structure, in terms of the presence and local density of states decay into vacuum of the empty surface state in band gap, and its effect on the tunnel current of the AlN(10 $\bar{1}0$) surface are analogous to those of the (Al,Ga)N and GaN (10 $\bar{1}0$) surfaces. Assuming this model, we simulate the tunnel current in the center of the AlN layer, farthest away from any interface, using the same procedure as outlined above for the ternary surfaces with adjusted materials parameter:

For pure AlN, the actual carrier concentration is significantly smaller than the Si doping concentrations due to compensation^{33–35,50–53} and a sharp increase of the activation energy for higher Al concentrations, reaching 250 meV for pure AlN^{33,34}. To take this effect into account, a doping concentration as low as $1 \cdot 10^{16} \text{ cm}^{-3}$ was assumed.

The such simulated AlN tunnel spectrum is shown as violet line in Fig. 2c and the respective band diagram in Fig. 3a. For this simulation the surface state position and the electron affinity are used as fit parameters. The simulation reproduces well the onsets and slopes at posi-

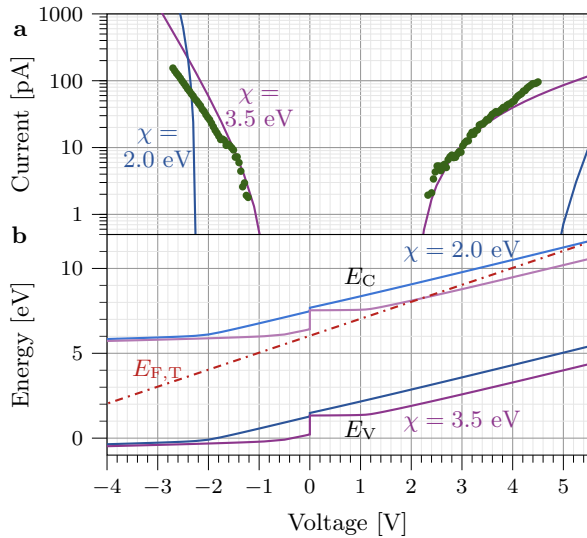


Figure 4. (a) Comparison of the $I(V)$ tunnel spectrum measured in the center of the AlN layer (spectrum number 1 in Fig. 2c) with simulated spectra assuming tunneling into bulk states only (and a doping concentration of $1 \cdot 10^{16} \text{ cm}^{-3}$). Two calculations are illustrated, which use electron affinities of $\chi = 2.0 \text{ eV}$ and $\chi = 3.5 \text{ eV}$. (b) Simulated positions of the conduction (light blue, violet) and valence (darker blue, violet) band edges at the surface as a function of applied voltage at the AlN surface for the two cases (see (a)). The Fermi level of the tip (red dashed-dotted line) is for low electron affinities inside the fundamental band gap for almost the whole simulated voltage range. At high electron affinities the Fermi level of the tip crosses the conduction band edge at roughly +2 V. The offset at 0 V is model based, since at negative voltages the surface state is almost instantaneously emptied and cannot be refilled. Thus, the upward band bending (or Fermi level pinning) due to the surface state cannot be maintained. The subtle kinks in the band edges at +1 V arise from the charging/discharging of the surface state due to tip-induced upward band bending.

tive and negative voltages. The onset at positive voltages is directly connected to the energy position of the empty surface state of $E_C - 1.4 \pm 0.4 \text{ eV}$.

However, the electron affinity needed for a reasonable agreement is rather large with 3.5 eV as compared to literature values ranging between 0.6 and 2 eV^{40,41,45–49}. Smaller electron affinities lead to much too large slopes of the negative tunnel current branch, due to the reduced tunneling barrier. Simultaneously, a lower electron affinity shifts the current onsets to larger absolute voltages due to a much larger contact potential between the tip and the AlN surface. Figure 4a illustrates this situation for an exemplary electron affinity of 2 eV. Note, ultimately, the Fermi level of the tip faces only energies within the fundamental band gap of AlN (Fig. 4b) and thus no states are present in the sample for elastic tunneling to tip states. This suppresses tunneling and results in a too wide apparent band gap, which is limited at negative voltages by tunneling from a tip-induced accumu-

lation zone in the AlN conduction band and at positive voltages by the crossing of the tip's Fermi level with the conduction band edge.

Therefore, we turn to an alternative tunneling model based on tunneling directly into and out of the AlN surface states. Since the filled and empty dangling bond surface states are in the fundamental band gap, the surface's band gap is effectively smaller and thus tunneling of electrons between the tip and the surface states becomes possible at much smaller voltages than tunneling into bulk states (see Fig. 3b). The onset voltage V_{onset} of tunneling into the empty dangling bond surface state is a function of the surface state's minimum energy position relative to the conduction band ($E_C - E_{\text{SS}}$) and the band bending at the surface (ϕ_{surf}):

$$E_C - E_{\text{SS}} = e(\phi_{\text{surf}} - V_{\text{onset}}) . \quad (1)$$

Using this model $E_C - E_{\text{SS}}$ can be deduced from the current onset measured in the experimental $I(V)$ spectra, provided that the surface band bending at the onset voltage is known. Since ϕ_{surf} is not directly accessible in STS experiments, it is calculated by solving the electrostatic potential of the tip-vacuum-semiconductor system.^{26–28}

The onset voltage of the positive current branch V_{onset} is experimentally extracted by fitting an exponential function $I \propto \exp(\alpha \cdot |V - V_{\text{onset}}|^{0.5})$ to the current values $I(V)$. This yields $V_{\text{onset}} = +1.8 \text{ V}$, which results into a surface state energy below the conduction band edge of $E_C - E_{\text{SS}} = (1.1 \pm 0.4) \text{ eV}$ for AlN (10 $\bar{1}$ 0). The error bar is estimated on basis of the accuracy of the determination of V_{onset} and a range of tip radii used in the calculation.⁵⁴ The calculations were done assuming a electron affinity of 2 eV for AlN as outlined above. If the electron affinity is smaller (e.g. 1.5 eV), the resulting surface state energy increase slightly (e.g. from 1.1 to 1.5 eV).

It is worth noting that dislocations intersect the m -plane cleavage surface of the different (Al,Ga)N layers, with decreasing concentrations along the growth direction. The dislocation cores can be anticipated to exhibit defect states in the band gap too. However, the density of dislocations is many orders of magnitude smaller than the density of intrinsic surface states.²⁴ Hence, the effect of dislocation states or their strain field can be neglected.

C. Comparison with DFT calculations

We now turn to a comparison with DFT calculations. For our DFT calculations with the Vienna Ab-initio Simulation Package (VASP)^{56,57}, we used the Heyd, Scuseria, and Ernzerhof hybrid functional with a mixing parameter a of 0.25 (HSE06),⁵⁸ projector augmented wave (PAW) potentials⁵⁹ and a planewave energy cutoff of 400 eV. Convergence with respect to energy cutoff, vacuum, and slab thickness was explicitly checked and found to provide surface energies with an accuracy better than 5 meV/ 1×1 . The Brillouin zone (BZ) was sampled using an equiva-

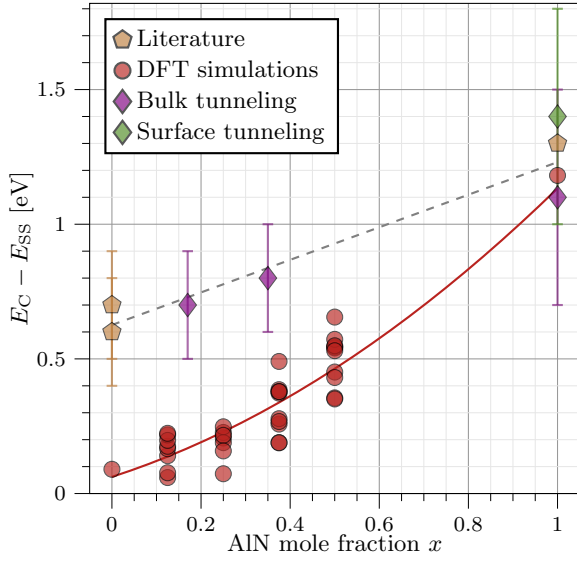


Figure 5. Energy of the minimum of the empty cation-derived surface dangling bond state relative to the conduction band edge for different Al compositions x of $\text{Al}_x\text{Ga}_{1-x}\text{N}(10\bar{1}0)$ surfaces. The red circles represent results from our DFT calculations. The violet (green) diamonds correspond to the surface state positions obtained from the measured tunneling spectra using simulation assuming tunneling into bulk bands only (tunneling into surface states of AlN only). Yellow pentagons represent literature values extracted from Ref.^{12,15,20} for GaN and from Ref.⁵⁵ for AlN.

lent $4 \times 4 \times 3$ Γ centered Monkhorst-Pack k-point mesh for the bulk primitive unit cell. The calculated fundamental band gaps ($E_C - E_V$) of binary bulk GaN and AlN are 3.09 and 5.59 eV, respectively.

With this methodology a total of six distinct AlGaIn alloy compositions were computed. For each composition, different configurations in a 16 atoms supercell having the primitive vectors along $\langle 1\bar{1}00 \rangle$, $\langle 11\bar{2}0 \rangle$, and $\langle 0001 \rangle$, have been constructed. The positions of the atoms were relaxed until all forces were less than 0.01 eV/Å. The lattice constants were determined by applying the Vegard's law, i.e., varied linearly with the composition. For the end constituents, the equilibrium lattice constants have been used.

To model the surfaces, the bulk supercells were repeated along the $\langle 1\bar{1}00 \rangle$ axis and slabs with 16 MLs thickness were constructed. For each configuration, the bulk was cleaved at four different planes to model different surface alloy configurations for the same composition and bulk configuration. The anion and cation dangling bonds at the bottom side of the slab were passivated by partially charged pseudohydrogens. Atoms in the four topmost layers were allowed to relax.

Figure 5 depicts the minimum of the cation-derived surface state relative to the bulk conduction band edge ($E_C - E_{SS}$) as obtained by the DFT calculations and experimentally. The surface state position obtained in DFT calculations is indicated by red circles. For pure GaN the

minimum of the surface state is calculated to be 0.1 eV below the bulk conduction band minimum. For higher Al contents the difference between the bulk conduction band edge and the minimum of the surface state increases until it reaches ≈ 1.2 eV for pure AlN. The experimentally obtained values are depicted as violet and green diamonds for tunneling into bulk and surface states respectively. The values found in literature for pure GaN^{12,15,20} and AlN⁵⁵ are shown as brown pentagons in Fig. 5.

The present DFT calculations overestimate the position of the dangling bond surface state with respect to the bulk valence band maximum (≈ 3 eV) (i.e. underestimate the energy difference between the empty dangling bond state and the bulk conduction band minimum) compared to previous reports: Both LDA+U⁵⁶ and LDA based modified pseudopotential⁵⁷ calculations predict the empty surface state at ≈ 2.7 eV above the bulk VBM. This difference can be attributed to the different methodologies and the alignment between the ternary alloys and AlN needed in the present case.

The errors on the experimental values for the energy minima of the surface state are primarily of statistical nature arising from the noise during acquisition of the tunneling spectra (see error bars in Fig. 2): The errors of the extracted surface state energy minima in Fig. 5 were derived by comparing the confidence range of the simulation (determined using variations of the surface state position in the simulation) with the experimental error bar range of the tunneling spectra (in Fig. 2). Agreement of both ranges yielded the final error bars in Fig. 5.

Hence, the calculated literature value for pure AlN and the present DFT calculation are in good agreement, and fit well with the surface state position determined experimentally here. Therefore, both the surface state position resulting from measurement and the one resulting from DFT calculation are in good agreement and reveal a weak shift of the surface state toward midgap with increasing Al concentration (and thus of the surface potential) of roughly $5 \cdot 10^{-3}$ eV/%. This trend is indicated by the gray dashed line in Fig. 5.

D. Spatial gradient of AlN electronic properties

Finally, we address the spatial dependence of the tunneling spectra within the AlN layer. Figure 6 illustrates the tunnel current in false colors versus voltage and spatial position. The current onsets appear as yellow-greenish color transition at both voltage polarities. Within the ternary (Al,Ga)N layers little changes occur. However, at the transition from the $\text{Al}_{0.35}\text{Ga}_{0.65}\text{N}/\text{AlN}$ interface the current onset increases at positive voltages continuously within the AlN layer over a spatial extension of roughly 150 nm. This effect is in line with the shifting positive current branches in Fig. 2c.

In order to identify the origin of the changes of the tunneling spectra within the AlN layer, we checked possible compositional fluctuations using SIMS. Except Ga

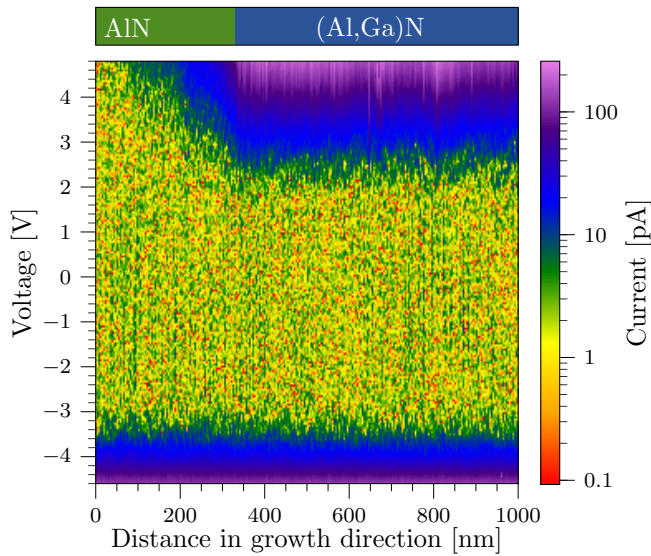


Figure 6. Evolution of tunnel spectra across the $\text{Al}_x\text{Ga}_{1-x}\text{N}/\text{AlN}$ interface along the growth direction: The spectra were measured using a negative setpoint of -4.5 V and 80 pA. The yellow-greenish color transitions at positive and negative voltages correspond to the respective current onsets, revealing the apparent band gap. A wide transition region of the positive current onset and thereby apparent band gap between AlN and $(\text{Al,Ga})\text{N}$ is visible.

no other element is found to have a concentration decay within the AlN layer. However, the highest Ga concentration within the AlN layer is smaller than 1% according to SIMS data and smaller than about 3% estimated on basis of the EDX data (Fig. 1). At these concentrations, the conductivity and free carrier density is not changing sufficiently to account for the changes in tunneling spectroscopy observed within the AlN layer.^{52,60} Thus Ga/Al interdiffusion can be ruled out as origin.

The spatial extension of the current onsets within the AlN of roughly 150 nm coincides however with the screening length within the AlN bulk visible in Fig. 3b. This suggests that the spatial variation reflects the screening of the built-in potential at the $\text{Al}_{0.35}\text{Ga}_{0.65}\text{N}/\text{AlN}$ interface and the different carrier concentrations in both layers.

V. CONCLUSION

We unravel the energy position of the group III-derived empty dangling bond surface state at non-polar $\text{Al}_x\text{Ga}_{1-x}\text{N}(10\bar{1}0)$ surfaces as a function of the Al concentration using cross-sectional scanning tunneling spectroscopy in conjunction with tunnel current simulations. The measurements show that the minimum energy of the empty dangling bond state shifts toward midgap with increasing Al concentration. The shift is in first approximation linear with a slope of ≈ 5 meV/%. These experimental findings are in good agreement with complementary DFT calculations, which reveal the same trend.

ACKNOWLEDGEMENT

This work was funded by the Deutsche Forschungsgemeinschaft (DFG, German Research Foundation) [grant number 398305088]. The authors thank Y. Wang, L. Zhang, and V. Assenmacher for help with the experiments.

AUTHOR DECLARATIONS

Conflict of Interest

The authors have no conflicts to disclose.

DATA AVAILABILITY

The data that support the findings of this study are available from the corresponding author upon reasonable request.

REFERENCES

- ¹A. I. Alhassan, R. M. Farrell, B. Saifaddin, A. Mughal, F. Wu, S. P. DenBaars, S. Nakamura, and J. S. Speck, *Opt. Express* **24**, 17868 (2016).
- ²T. Fujiwara, S. Rajan, S. Keller, M. Higashiwaki, J. S. Speck, S. P. DenBaars, and U. K. Mishra, *Appl. Phys. Expr.* **2**, 011001 (2009).
- ³A. Dadgar, A. Strittmatter, J. Bläsing, M. Poschenrieder, O. Contreras, P. Veit, T. Riemann, F. Bertram, A. Reiher, A. K. K. Diez, T. Hempel, T. Finger, A. Kasic, M. Schubert, D. Bimberg, F. A. Ponce, J. Christen, and A. Krost, *Phys. Status Solidi C* **0**, 1583 (2003).
- ⁴Y. Sun, K. Zhou, Q. Sun, J. Liu, M. Feng, Z. Li, Y. Zhou, L. Zhang, D. Li, S. Zhang, M. Ikeda, S. Liu, and H. Yang, *Nat. Photonics* **10**, 595 (2016).
- ⁵R. Xiang, Y.-Y. Fang, J. Dai, L. Zhang, C. Su, Z. Wu, C. Yu, H. Xiong, C. Chen, and Y. Hao, *J. Alloys Comp.* **509**, 2227 (2011).
- ⁶J. Cheng, X. Yang, L. G. Ling Sang, J. Zhang, J. Wang, C. He, L. Zhang, M. Wang, F. Xu, N. Tang, Z. Qin, X. Wang, and B. Shen, *Sci. Rep.* **6**, 23020 (2016).
- ⁷C. E. Dreyer, A. Janotti, C. G. Van de Walle, and D. Vanderbilt, *Phys. Rev. X* **6**, 021038 (2016).
- ⁸P. Waltereit, O. Brandt, A. Trampert, H. T. Grahn, J. Menniger, M. Ramsteiner, M. Reiche, and K. H. Ploog, *Nature* **406**, 865 (2000).
- ⁹V. N. Bessolov, E. V. Konenkova, S. A. Kukushkin, A. V. Osipov, and S. N. Rodin, *Rev. Adv. Mat. Sci.* **38** (2014).
- ¹⁰V. Bermudez, *Surf. Sci. Rep.* **72**, 147 (2017).
- ¹¹L. Janicki, J. Misiewicz, G. Cywiński, M. Sawicka, C. Skierbiszewski, and R. Kudrawiec, *Appl. Phys. Express* **9**, 021002 (2016).
- ¹²L. Lympirakis, P. H. Weidlich, H. Eisele, M. Schnedler, J.-P. Nys, B. Grandier, D. Stievenard, R. E. Dunin-Borkowski, J. Neugebauer, and Ph. Ebert, *Appl. Phys. Lett.* **103**, 152101 (2013).
- ¹³M. Himmerlich, A. Eisenhardt, S. Shokhovets, S. Krischok, J. Räthel, E. Speiser, M. D. Neumann, A. Navarro-Quezada, and N. Esser, *Appl. Phys. Lett.* **104**, 171602 (2014).
- ¹⁴M. Landmann, E. Rauls, W. G. Schmidt, M. D. Neumann, E. Speiser, and N. Esser, *Phys. Rev. B* **91**, 035302 (2015).

- ¹⁵M. Schnedler, V. Portz, H. Eisele, R. E. Dunin-Borkowski, and Ph. Ebert, *Phys. Rev. B* **91**, 205309 (2015).
- ¹⁶S. Nayak, M. H. Naik, M. Jain, U. V. Waghmare, and S. M. Shivaprasad, *J. Vac. Sci. Technol. A* **38**, 063205 (2020).
- ¹⁷X. Cai, Y. Ma, J. Ma, D. Xu, and X. Luo, *Phys. Chem. Chem. Phys.* **23**, 5431 (2021).
- ¹⁸K. Sagisaka, O. Custance, N. Ishida, T. Nakamura, and Y. Koide, *Phys. Rev. B* **106**, 115309 (2022).
- ¹⁹L. Lymperakis, J. Neugebauer, M. Himmerlich, S. Krischok, M. Rink, J. Kröger, and V. M. Polyakov, *Phys. Rev. B* **95**, 195314 (2017).
- ²⁰C. G. Van de Walle and D. Segev, *J. Appl. Phys.* **101**, 081704 (2007).
- ²¹L. Janicki, M. Ramirez-López, J. Misiewicz, G. Cywiński, M. Boćkowski, G. Muziol, C. Chèze, M. Sawicka, C. Skierbiszewski, and R. Kudrawiec, *Jap. J. Appl. Phys.* **55**, 05FA08 (2016).
- ²²H. Eisele, J. Schuppang, M. Schnedler, M. Duchamp, C. Nenstiel, V. Portz, T. Kure, M. Bügler, A. Lenz, M. Dähne, A. Hoffmann, S. Gwo, S. Choi, J. S. Speck, R. E. Dunin-Borkowski, and Ph. Ebert, *Phys. Rev. B* **94**, 245201 (2016).
- ²³V. Portz, M. Schnedler, L. Lymperakis, J. Neugebauer, H. Eisele, J.-F. Carlin, R. Butté, N. Grandjean, R. E. Dunin-Borkowski, and P. Ebert, *Appl. Phys. Lett.* **110**, 022104 (2017).
- ²⁴L. Zhang, V. Portz, M. Schnedler, L. Jin, Y. Wang, X. Hao, H. Eisele, R. E. Dunin-Borkowski, and Philipp Ebert, *Philos. Mag.* **98**, 3072 (2018).
- ²⁵Ernst Ruska-Centre for Microscopy and Spectroscopy with Electrons (ER-C), *Journal of large-scale research facilities* **2**, A43 (2016).
- ²⁶M. Schnedler, V. Portz, P. H. Weidlich, R. E. Dunin-Borkowski, and Ph. Ebert, *Phys. Rev. B* **91**, 235305 (2015).
- ²⁷M. Schnedler, R. E. Dunin-Borkowski, and Ph. Ebert, *Phys. Rev. B* **93**, 195444 (2016).
- ²⁸M. Schnedler, *P-SpaceChargeLight* (April 2021), https://github.com/mschnedler/P_SpaceChargeLight (retrieved, June 2021).
- ²⁹J. R. Chelikowsky and M. L. Cohen, *Phys. Rev. B* **20**, 4150 (1979).
- ³⁰W. Götz, N. M. Johnson, C. Chen, H. Liu, C. Kuo, and W. Imler, *Appl. Phys. Lett.* **68**, 3144 (1996).
- ³¹C. G. Van de Walle, C. Stampfl, and J. Neugebauer, *J. Cryst. Growth* **189-190**, 505 (1998).
- ³²H. Wang and A.-B. Chen, *J. Appl. Phys.* **87**, 7859 (2000), <https://doi.org/10.1063/1.373467>.
- ³³R. Collazo, S. Mita, J. Xie, A. Rice, J. Tweedie, R. Dalmau, and Z. Sitar, *Phys. Status Solidi C* **8**, 2031 (2011).
- ³⁴I. S. Bryan, *Al-rich AlGa_N and AlN Growth on Bulk AlN Single Crystal Substrates*, Ph.D. thesis, North Carolina State University (2015).
- ³⁵I. Bryan, Z. Bryan, S. Washiyama, P. Reddy, B. Gaddy, B. Sarkar, M. H. Breckenridge, Q. Guo, M. Bobea, J. Tweedie, S. Mita, D. Irving, R. Collazo, and Z. Sitar, *Appl. Phys. Lett.* **112**, 062102 (2018), <https://doi.org/10.1063/1.5011984>.
- ³⁶K. Besocke and H. Wagner, *Phys. Rev. B* **8**, 4597 (1973).
- ³⁷C. J. Fall, N. Binggeli, and A. Baldereschi, *Phys. Rev. B* **65**, 045401 (2001).
- ³⁸S. Loth, M. Wenderoth, R. G. Ulbrich, S. Malzer, and G. H. Döhler, *Phys. Rev. B* **76**, 235318 (2007).
- ³⁹A. P. Wijnheijmer, J. K. Garleff, M. A. v. d. Heijden, and P. M. Koenraad, *J. Vac. Sci. Technol. B* **28**, 1086 (2010).
- ⁴⁰T. Kozawa, T. Mori, T. Ohwaki, Y. Taga, and N. Sawaki, *Jpn. J. Appl. Phys.* **39**, L772 (2000).
- ⁴¹S. P. Grabowski, M. Schneider, H. Nienhaus, W. Mönch, R. Dimitrov, O. Ambacher, and M. Stutzmann, *Appl. Phys. Lett.* **78**, 2503 (2001).
- ⁴²P. Reddy, I. Bryan, Z. Bryan, J. Tweedie, S. Washiyama, R. Kirste, S. Mita, R. Collazo, and Z. Sitar, *Appl. Phys. Lett.* **107**, 091603 (2015), <https://doi.org/10.1063/1.4930026>.
- ⁴³V. Portz, M. Schnedler, H. Eisele, R. E. Dunin-Borkowski, and Ph. Ebert, *Phys. Rev. B* **97**, 115433 (2018).
- ⁴⁴L. Lymperakis (2021).
- ⁴⁵V. M. Bermudez, T. M. Jung, K. Doverspike, and A. E. Wickenden, *J. Appl. Phys.* **79**, 110 (1996).
- ⁴⁶C. I. Wu, A. Kahn, E. S. Hellman, and D. N. E. Buchanan, *Appl. Phys. Lett.* **73**, 1346 (1998).
- ⁴⁷C. I. Wu and A. Kahn, *Appl. Phys. Lett.* **74**, 546 (1999).
- ⁴⁸P. G. Moses, M. Miao, Q. Yan, and C. G. Van de Walle, *J. Chem. Phys.* **134**, 084703 (2011).
- ⁴⁹P. Strak, P. Kempisty, K. Sakowski, and S. Krukowski, *J. Vac. Sci. Technol. A* **35**, 021406 (2017), <https://doi.org/10.1116/1.4975332>.
- ⁵⁰Y. Taniyasu, M. Kasu, and N. Kobayashi, *Appl. Phys. Lett.* **81**, 1255 (2002), <https://doi.org/10.1063/1.1499738>.
- ⁵¹Y. Shimahara, H. Miyake, K. Hiramatsu, F. Fukuyo, T. Okada, H. Takaoka, and H. Yoshida, *Jpn. J. Appl. Phys.* **50**, 095502 (2011).
- ⁵²F. Mehnke, T. Wernicke, H. Pingel, C. Kuhn, C. Reich, V. Kueller, A. Knauer, M. Lapeyrade, M. Weyers, and M. Kneissl, *Appl. Phys. Lett.* **103**, 212109 (2013), <https://doi.org/10.1063/1.4833247>.
- ⁵³J. S. Harris, J. N. Baker, B. E. Gaddy, I. Bryan, Z. Bryan, K. J. Mirrieles, P. Reddy, R. Collazo, Z. Sitar, and D. L. Irving, *Appl. Phys. Lett.* **112**, 152101 (2018), <https://doi.org/10.1063/1.5022794>.
- ⁵⁴L. Freter, *Surface states and Fermi-level pinning on non-polar binary and ternary (Al,Ga)N surfaces*, Ph.D. thesis, RWTH Aachen University, Jülich (2022), english.
- ⁵⁵M. S. Miao, A. Janotti, and C. G. Van de Walle, *Phys. Rev. B* **80**, 155319 (2009).
- ⁵⁶G. Kresse and J. Furthmüller, *Phys. Rev. B* **54**, 11169 (1996).
- ⁵⁷G. Kresse and J. Furthmüller, *Comput. Mat. Sci.* **6**, 15 (1996).
- ⁵⁸J. Heyd, G. E. Scuseria, and M. Ernzerhof, *J. Chem. Phys.* **124**, 10.1063/1.2204597 (2006), 219906, https://pubs.aip.org/aip/jcp/article-pdf/doi/10.1063/1.2204597/15387022/219906.1_online.pdf.
- ⁵⁹P. E. Blöchl, *Phys. Rev. B* **50**, 17953 (1994).
- ⁶⁰P. Pampili and P. J. Parbrook, *Mat. Sci. Semicond. Process.* **62**, 180 (2017).